PAPER

Check for updates

Redox-driven synthesis of stable copper nanoparticles *via* metal displacement and their application in organic dye degradation

Rajanikumar Kandikonda,[a] Govindhasamy Murugadoss,[b] Nachimuthu Venkatesh,[b] Siva Shankari Velmurugan Subbaraj, [ID][c] Divya Palani,[c] Suneetha Thota,[d] Rakesh Kumar Rajaboina, [ID][a] Haranath Divi, [ID][a] Manikandan Dhayalan, [ID]*[e] Anuchit Phanumartwiwath,*[e] Chenna Reddy Mallu [ID]*[d] and Uday Kumar Khanapuram [ID]*[a]

This study uses a novel approach to synthesize copper nanoparticles (Cu NPs) using tartaric acid as a reducing and capping agent *via* a metal displacement method. The uniqueness of this approach lies in its clean and efficient synthesis route that enables the formation of metallic copper nanoparticles under mild conditions by employing tartaric acid as a dual-functioning complexing and capping agent, and utilizing a spontaneous metal displacement reaction with aluminum. The quality of the synthesized Cu NPs is clearly reflected in the characterization results, which show an average size of 3 nm, sharp crystallinity (crystallite size around 32 nm), the absence of oxide phases, and strong surface functionalization, confirming the successful formation of stable, oxidation-resistant metallic copper. This approach stands out for producing structurally pure and chemically intact Cu^0 nanoparticles without relying on toxic chemicals or inert environments. Evaluation of the photocatalytic activity of the Cu NPs by monitoring the degradation of sample pollutants under visible light irradiation revealed their exceptional efficiency in the removal of organic contaminants from wastewater. The localized surface plasmon resonance (LSPR) effect is a unique property of copper nanoparticles that enables them to absorb visible light, further making them an auspicious material for photocatalytic applications. The synthesized Cu nanoparticle photocatalyst exhibited excellent visible-light-driven degradation efficiencies of 97.9% for rose bengal ($k = 0.043$ min^{-1}) and 88.0% for methylene blue ($k = 0.026$ min^{-1}). These results highlight its strong photocatalytic performance and favorable reaction kinetics. This synthesis strategy offers a sustainable route to producing high-quality copper nanomaterials with promising applications in environmental remediation and advanced photocatalytic systems.

1. Introduction

The looming threat of freshwater scarcity, exacerbated by rapid population growth, unsustainable urbanization, and climate change, underscores the urgent need for innovative solutions in water treatment.[1] As the world population is projected to reach 9.7 billion by 2050, the demand for freshwater resources will increase.[2,3] It is crucial to develop groundbreaking solutions that can minimize this strain and ensure unbiased access to safe and hygienic water for all.[4–6] The fact here is that water quality degradation poses significant environmental and health risks, with various types of contaminants in wastewater acting as major factors. These pollutants can be classified as organic, inorganic, and biological toxins, each having unique properties and potential impacts on aquatic ecosystems and human health.[7–9] Wastewater treatment is commonly carried out using a variety of approaches, including physical, chemical, and biological treatment approaches.[10–13]

Heterogeneous photocatalysis is a promising process for enhanced oxidation, and this process utilizes light energy on

[a] Energy Materials and Devices (EMD) Laboratory, Department of Physics, National Institute of Technology, Warangal 506004, Telangana, India.
E-mail: kanapuram.udaykumar@nitw.ac.in

[b] Centre for Nanoscience and Nanotechnology, Sathyabama Institute of Science and Technology, Chennai 600 119, Tamil Nadu, India

[c] Centre for Waste Management, Sathyabama Institute of Science and Technology, Chennai 600 119, Tamil Nadu, India

[d] Department of Chemistry, Freshman Engineering, Geethanjali College of Engineering and Technology, Hyderabad, Telangana, India.
E-mail: malluchennareddypvc@gmail.com

[e] College of Public Health Sciences (CPHS), Chulalongkorn University, Bangkok, 10330, Thailand. E-mail: manikandandhayalan88@gmail.com, anuchit.p@chula.ac.th

semiconductor or metal nanoparticles to facilitate pollutant degradation in wastewater.[14–18] Copper nanoparticles (Cu NPs) have attracted momentous attention for their potential applications in photocatalysis due to their unique optical and electronic properties.[19] The localized surface plasmon resonance (LSPR) effect is a unique property of copper nanoparticles that enables them to absorb visible light, further making them an auspicious material for photocatalytic applications.[20–23] Studies have established the ability of copper nanoparticles to degrade a variety of pollutants, including pesticides, industrial chemicals, and organic dyes, over a period of time under different conditions.[24–27] By adapting the surface, shape and size properties of copper nanoparticles to optimize for more efficient pollutant degradation, photocatalytic performance can be optimized.[28]

CuNPs are appealing alternatives to noble metal-based catalysts, offering advantages such as visible-light plasmonic activation, low material cost, excellent electrical conductivity, and excellent environmental stability. Unlike typical semiconductor-based catalysts (e.g., TiO_2, ZnO, and CdS), Cu nanoparticles can generate Reactive oxygen species (ROS) through a plasmonic mechanism, eliminating the need for complex doping or heterojunction engineering.[29] However, their high reactivity causes rapid surface oxidation in ambient conditions, forming Cu_2O or CuO, which greatly reduces their functional properties.[30,31] This inherent instability poses a significant challenge to their application in practical settings, such as flexible electronics, catalysis, and sensors.[32–34] To overcome this, surface capping and stabilization strategies have been widely studied, including polymer encapsulation and ligand coordination, chemical reduction using agents such as sodium borohydride and ascorbic acid, green synthesis with plant extracts, and stabilization with polymers like poly(tartaric acid).[35–39] Despite their utility, these methods often face limitations such as particle aggregation, susceptibility to oxidation, and complex processing steps, which hinder scalability and long-term stability. As an alternative, metal displacement reactions offer a simple, scalable, and environmentally benign route for producing metallic nanoparticles.[40–42] In such systems, more electropositive metals such as zinc or aluminum can spontaneously reduce Cu^{2+} ions through galvanic exchange.[42,43] This principle has been utilized to deposit copper onto aluminum substrates or to generate Cu NPs in situ. More complex approaches, such as double-atom (heteroatom) displacement involving sequential Au/Cu ion exchange in alloy clusters, have also been investigated for the precision-controlled synthesis of nanoparticles.

Notably, citrate-capped Cu NPs studied by Yoon et al. demonstrated remarkable mechanical durability, maintaining electrical conductivity even after 2500 bending cycles, which highlights the importance of surface chemistry in protecting against oxidation.[44] Despite these advances, current methods often require harsh chemical reductants or complex reaction conditions, or are difficult to scale up. In contrast, we present for the first time an easy, eco-friendly, and scalable method for making tartaric acid-capped metallic Cu NPs through single-atom metal displacement using aluminium scrap as a reductant in a tartaric acid solution. To the best of our knowledge, single-atom displacement in tartaric acid has not been reported, particularly with the aid of ultrasonic activation to enhance reaction kinetics and nanoparticle dispersion.[45] The reaction is improved by ultrasonic activation, which ensures even dispersion and speeds up ion exchange. Tartaric acid acts not only as the reaction medium but also as a surface-capping agent, effectively preventing oxidation.[35] The resulting Cu NPs demonstrate excellent oxidation stability, keeping their crystalline metallic phase with minimal CuO formation even after 45 days of air exposure, confirmed by transmission electron microscopy (TEM) analysis. This method provides a new and sustainable way to produce oxidation-resistant Cu NPs, ideal for next-generation nanomaterial-based devices. The synthesized Cu NPs are used to characterize and assess their application in wastewater treatment, particularly in the degradation of organic pollutants. By exploring the potential of Cu NPs in wastewater treatment, this study aims to contribute to the development of efficient and cost-effective solutions for environmental remediation.

2. Experimental methods

2.1. Materials & methods

All chemical reagents, including copper sulphate ($CuSO_4$), and tartaric acid, were purchased from Sigma-Aldrich and used as received. All the chemicals used were of the highest purity available. Ultrapure water (DM water) was used for all the experiments.

2.2. Metal displacement synthesis of Cu NPs

The Cu NP synthesis was carried out by using a green and facile redox metal displacement method involving tartaric acid and aluminum scrap as key reagents; the detailed flowchart is presented in Fig. 1. Initially, 100 g of tartaric acid was dissolved in 100 mL of DM water, forming a transparent tartaric acid solution with a pH of 2.77. This acidic medium facilitates the complexation of Cu^{2+} ions and tartrate ligands. Separately, copper sulfate pentahydrate ($CuSO_4 \cdot 5H_2O$) with particle sizes of 40–60 μm was dissolved in DM water and then added to the tartaric solution. The mixture was stirred continuously for 30 minutes, during which a copper–tartrate complex was formed, raising the solution's pH to 3.46. This complexation step is critical as it modulates the redox potential of Cu^{2+} ions and ensures controlled nucleation during reduction. Furthermore, aluminum scrap was introduced as a reducing agent into the copper–tartrate complex. Since aluminum scrap is more electropositive, Cu^{2+} ions were spontaneously reduced to metallic copper, while aluminum was oxidized to Al^{3+}. The synthesized Cu NP photograph is presented in Fig. 1.

To speed up ion exchange and promote uniform nucleation, the mixture was subjected to ultrasonic agitation for 15 minutes. The ultrasonic waves broke apart agglomerates, increased the local temperature, and enhanced mass transport, resulting in a faster and more even reduction of copper ions into
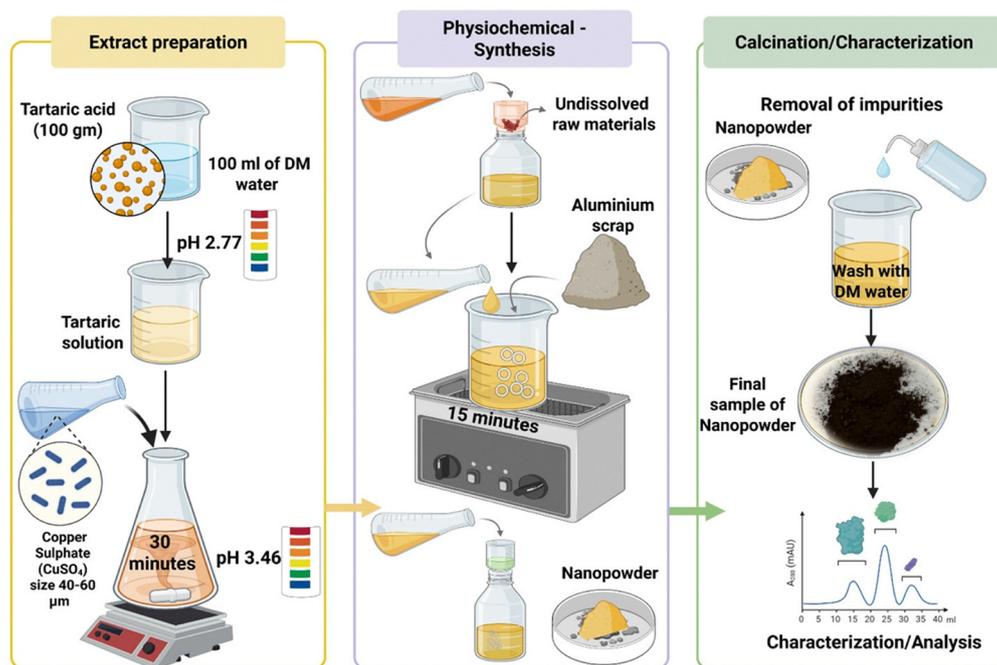
Fig. 1 Flowchart showing the metal displacement synthesis of Cu NPs.

nanoparticles. During this process, zero-valent copper atoms nucleated and grew into nanoscale clusters. Tartaric acid molecules served a dual role: they stabilized the copper nuclei through electrostatic and steric interactions and also capped the nanoparticle surfaces to prevent aggregation and oxidation. This capping process involved the coordination of hydroxyl and carboxyl groups from tartaric acid with the copper surface. After approximately 30 minutes, the reddish-brown Cu NPs precipitated and settled at the bottom of the vessel. The solid product was isolated from the reaction mixture through filtration and was thoroughly washed several times with deionized water to remove any leftover aluminum ions, unreacted precursors, and byproducts. The detailed mechanism of the Cu NPs is illustrated in Fig. 2. After purification, the copper nanopowder was collected and air-dried. This process finalized the synthesis, producing stable, dispersible Cu NPs ready for use in photocatalysis and environmental cleanup.

2.3. Characterization techniques

Various analytical techniques have been used for the characterization of metal displacement in the synthesized Cu NPs. The morphological and elemental characterization was performed using TEM, JEM-2100plus, JEOL Japan, 0.2 Å resolution. The crystal structure was determined through X-ray diffraction (XRD) using a SMART LAB 9 kW system (Rigaku, Japan). X-Ray photoelectron spectroscopy (XPS) was performed using a Thermo Fisher Scientific, Model-K-Alpha, aluminium (Al) K-alpha micro-focused monochromator, energy resolution ≤0.5 eV, pass energy-50.0 eV for high resolution scan, pass energy – 200.0 eV for survey scan, energy step size – 0.1 eV, X-ray power – 72 W, analyzer – 180° double-focusing hemispherical

analyzer, detector – 128-channel detector. The Brunauer–Emmett–Teller (BET) method was utilized for surface area analysis using an Anton Paar Autosorb iQ Station. Diffuse reflectance UV-VIS spectra of the samples were recorded using a UV-Vis NIR spectrophotometer (Agilent Technology, Carry 5000). The structural features were analyzed using Fourier transform infrared spectroscopy (FTIR) (Shimadzu 8201 PC Fourier Transform Infrared). Raman spectroscopic studies were performed using a Horiba Jobin Yvon, LABRAM-HR.

Photocatalytic study. Photodegradation of organic dyes like methylene blue (MB), rose bengal (RB), and a mixed dye of MB and RB by using the prepared catalysts. These carcinogenic dyes are harmful to the environment, and to break these dye molecules to reduce their toxicity, we have selected photocatalytic dye degradation with Cu NPs. In this experimental process, 25 mg of the generated catalysts was dissolved in 50 mL of dye solution (20 mg L^{-1}). Later catalysts containing dye solution were exposed to the visible light by using a photoreactor (Annular type-250 W tungsten lamp) for 3 hours. During light irradiation, 1.5 mL of dye solution was collected at fixed intervals of time from the photoreactor for intensity measurement with a UV-Visible spectrophotometer (Systronics-2203double beam spectrophotometer). The maximum absorbance for MB & RB was 663 nm and 545 nm, respectively. The formula for calculating the degradation efficiency is,

$$\text{Degradation efficiency } (\%) = \frac{C_0 - C}{C_0} \times 100. \qquad (1)$$

where C_0 and C are the initial and variable intensities of the dye molecules, respectively, and the treated sample was centrifuged following the first cycle to finish the stability study, cleaned with acetone and water, and dried at 80 °C.[46,47] Additionally, to
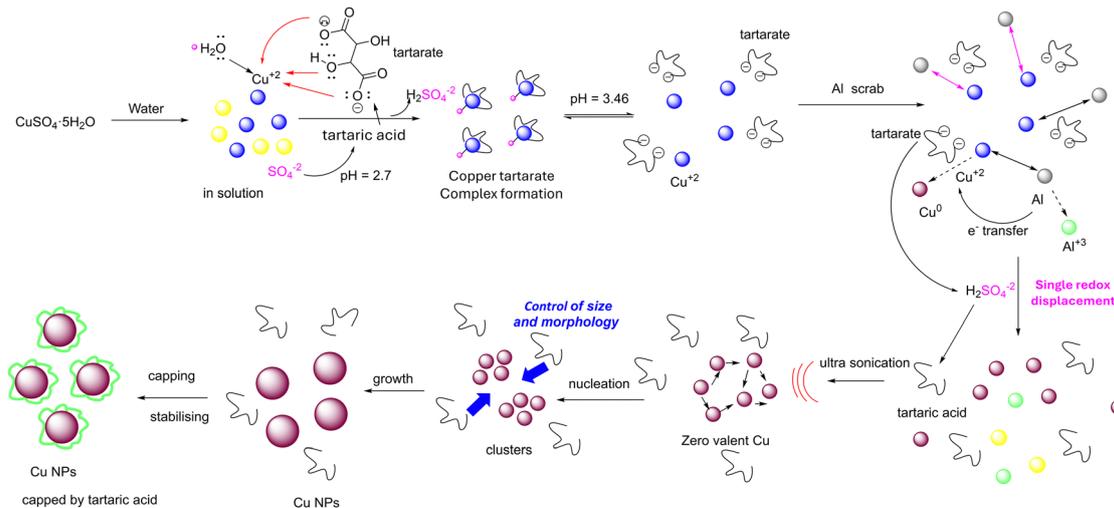
Fig. 2 Illustration of the detailed steps of the Cu NP synthesis method.

determine the true depolluting rate, the following first-order kinetic investigation was conducted as follow as,

$$-\ln\left(\frac{c}{c_0}\right) = kt \tag{2}$$

where k (min^{-1}) is the rate of reaction constant and t (min) is time.[48,49] The photocatalytic research was conducted in a photoreactor with visible light and the light intensity was measured with a Digital Lux meter. As a result, the average light intensity was 0.80×10^5 lux, computed at 30-minute intervals.

3. Results & discussion

3.1. Characterization of MD Cu-NPs

The XRD analysis of the synthesized Cu NPs reveals a face-centered cubic (FCC) structure, consistent with the standard data (JCPDS 04-0836).[50,51] The diffraction peaks at 43.3°, 50.4°, and 74.1° correspond to the (111), (200), and (220) planes, respectively, indicating a high degree of crystallinity (shown in Fig. S1).[50,52,53] The absence of impurity peaks (CuO/Cu$_2$O) confirms the pristine phase of the nanoparticles, suggesting that the tartaric acid reduction method employed in this study is effective in producing pure Cu NPs.[54,55] The effectiveness of tartaric acid as a reducing and capping agent is evident in the XRD results, which show no signs of oxidation or impurities.

We observed remarkable stability of our synthesized Cu NPs against oxidation in air. To evaluate their stability, 1 g of the Cu NPs was exposed to air for a short duration (2 min) and then stored for 45 days, followed by a brief air exposure before sealing the vial. XRD analysis (Fig. S1) after 45 days revealed the exceptional stability of the Cu NPs. This can be attributed to the capping of Cu NPs with tartaric acid during synthesis, which likely prevented extensive oxidation.

The observed XRD data of the prepared Cu nanoparticles at room temperature are refined using the Rietveld refinement method with FullProf software (Fig. 3(a)). The data is refined by assuming the space group $Fm\overline{3}m$ and a cubic crystal structure.

The observed lattice parameters and the Rietveld refined parameters are given in Table 1. From the refinement of the observed data, there are no external impurities present in the prepared material, indicating high-purity single-phase cubic nanoparticles.[56,57] To estimate the crystallite size of the Cu nanoparticles, the Debye–Scherrer formula is used.

$$D = \frac{k\lambda}{\beta\cos\theta}$$

where $k \sim 0.89$ is the shape factor, $\lambda = 0.1542$ nm is the wavelength of Cu Kα radiation, β is the full width at half maxima (FWHM) of the peak and θ is the Bragg's angle. The calculated crystallite size is given in Table 1.

The FTIR spectrum of the synthesized Cu NPs reveals distinct vibrational bands corresponding to the functional groups of tartaric acid, confirming its role as an effective capping and stabilizing agent. As shown in Fig. 3(b), prominent bands at 3426 cm^{-1}, 2930 cm^{-1}, and 2854 cm^{-1} are attributed to O–H and sp^3 C–H stretching vibrations, while the strong band at 1625 cm^{-1} corresponds to the C=O stretching of carboxylic acid or carboxylate groups. Additional bands at 1361 cm^{-1} and 1022 cm^{-1} are assigned to C–O–C bending and C–O stretching vibrations, respectively.[44,53] These features are consistent with tartaric acid adsorption on the nanoparticle surface, forming a protective organic shell. Importantly, no absorption bands are observed in the region of 500–650 cm^{-1}, which typically indicates Cu–O bond vibrations associated with copper oxides (CuO or Cu$_2$O). This absence of oxide-related bands strongly suggests that the nanoparticles are predominantly metallic copper with no significant formation of oxides.[30] Compared with literature reports, the observed spectrum closely matches those of pure Cu NPs capped with organic acids and clearly differs from CuO or Cu$_2$O nanoparticles, which exhibit strong metal–oxygen bond vibrations in the low-frequency region. Thus, the FTIR analysis, in conjunction with supporting XRD, confirms the successful synthesis of phase-pure, metallic Cu NPs with long-term stability.
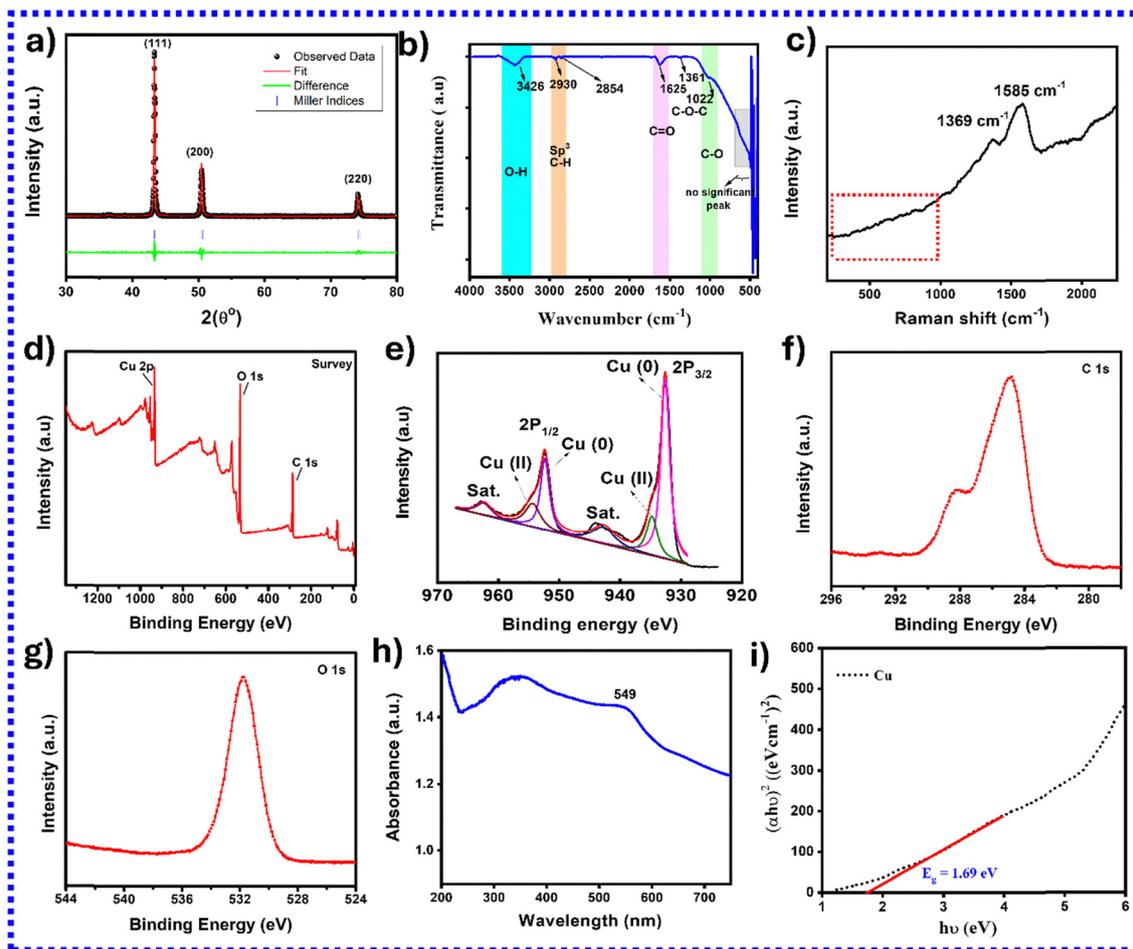
Fig. 3 Comprehensive characterization of the synthesized CuNPs: (a) XRD patterns of Cu NPs immediately after synthesis and after 45 days. (b) FTIR spectrum. (c) Raman spectrum. (d)–(g) XPS survey spectrum identifying Cu, O, and C elements in the sample. (h) UV-Visible absorption spectrum. (i) Tauc plot for bandgap evaluation.

Table 1 Refined crystallographic parameters and crystallite size of Cu nanoparticles obtained from Rietveld analysis of the XRD data. (R_p (profile residual), R_{wp} (weighted profile residual), GoF (goodness of fit), χ^2 (Chi-square): statistical indicator of fit, crystallite size (nm)

Lattice parameters ($a = b = c$)	R_p	R_{wp}	GoF	χ^2	Crystallite size (nm)
3.6151(2)	10.7	16.2	1.6	2.44	32

The Raman spectrum of the synthesized Cu NPs reveals two prominent peaks at 1369 cm^{-1} and 1585 cm^{-1}, which are attributed to the vibrational modes of surface-bound organic groups derived from tartaric acid (as shown in Fig. 3(c)). The peak at 1369 cm^{-1} corresponds to symmetric C–C stretching, while the 1585 cm^{-1} band is indicative of C=O or aromatic-type C=C stretching, both of which are characteristic of carboxylate and hydroxyl functionalities present in tartaric acid molecules.[58] These features confirm the successful surface functionalization of Cu NPs by tartaric acid, which acts as a capping and stabilizing agent. Importantly, no significant peaks are observed in the low-wavenumber region between 200 and 700 cm^{-1}, particularly around 280–630 cm^{-1}, where Cu–O vibrational modes typically appear in the CuO and Cu$_2$O nanoparticles.[59,60] This absence of Cu–O signals strongly supports the conclusion that the synthesized nanoparticles are predominantly metallic copper, free from oxide contamination.

The XPS studies of the synthesized Cu NPs were performed to determine the elemental composition and the chemical state. The results are depicted in Fig. 3(d)–(g). The survey spectra in Fig. 3(d) revealed the presence of Cu2p, O1s, and C1s. The deconvolution of the Cu2p spectrum in Fig. 3(e) showed that core level photoelectrons appear at BE of 932.5 eV and 934.7 eV corresponding to Cu(0) 2p$_{3/2}$ and Cu(II) 2p$_{3/2}$, respectively, along with the satellite peak at 943.4 eV.[61] The additional two other peaks are attributed to Cu(0) 2p$_{1/2}$ and Cu(II) 2p$_{1/2}$ photoelectrons that appear at binding energies of 952.45 eV and 954.4 eV, respectively, along with an associated satellite peak at 962.6 eV. The Cu(0) 2p$_{3/2}$ and Cu(0) 2p$_{1/2}$ peaks show a narrow FWHM of 1.7, confirming the successful formation of Cu metallic nanoparticles.[62] Relative atomic% for Cu(0) *vs.* Cu(II) has been calculated from the area of the peaks, and the results are 80:20, respectively. The Cu 2p$_{3/2}$ and Cu

2p$_{1/2}$, are well-separated with spin–orbit coupling of ∼20 eV. The shakeup satellite peaks are attributed to the 3d–4s transition during the ejection of 2p photoelectrons.[63] These XPS data confirm the successful formation of Cu metallic nanoparticles, which is also in agreement with the PXRD data. The C 1s and O 1s spectra, as shown, are attributed to C–O, C═O, C–C, and C–H from the capping agent tartaric acid, which also agrees well with FTIR data.

The UV-Visible spectrum of the synthesized Cu NPs exhibits a prominent surface plasmon resonance (SPR) absorption band centered at 549 nm, indicating the formation of metallic Cu NPs (shown in Fig. 3(h)). This SPR peak is a signature of collective oscillation of conduction electrons in response to incident light and is characteristic of nanoscale metallic copper, typically observed in the 540–580 nm range.[36,64,65] The band of Cu NPs was calculated using the Tauc plot from UV-Vis spectroscopy measurements (Fig. 3(i)). The calculated band gap was found to be 1.69 eV. It is well-known that colloidal Cu NPs of ∼10 nm exhibit well-defined SPR bands at around 555 nm, attributed to dipolar plasmon resonance, whereas oxidized copper forms (Cu$_2$O and CuO) exhibit broad, featureless absorptions either in the UV or near-IR region without such distinct SPR features.[64] The location and sharpness of the SPR band in our spectrum indicate high crystallinity, minimal surface oxidation, and a relatively narrow size distribution of the particles.

In the green synthesis approach described by Issaabadi et al. Cu NPs synthesized using *Thymus vulgaris* extract exhibited SPR peaks at approximately 560–570 nm, with a slight red shift attributed to a larger particle size and partial surface oxidation.[66] Similarly, Suramwar et al. reported that pure, starch-capped metallic Cu NPs prepared under ambient conditions exhibited SPR bands at 590 nm, while emphasizing that this absorption shifts to higher wavelengths in the presence of oxidation or aggregation.[67] Compared to these, our Cu NP peak at 549 nm is slightly blue-shifted, which suggests a smaller average particle size, reduced aggregation, and better resistance to oxidation, likely due to the effective capping action of tartaric acid in our method.[68,69] The absence of any secondary peaks in the UV region (∼300–400 nm) further rules out the presence of Cu$_2$O or CuO impurities, which typically exhibit characteristic interband transitions in that region.[70]

3.2. Morphological studies

TEM images have shown the size and distribution of the particles (Fig. 4(a) and (b)). It's revealed that the spherical nanosized particles and relatively narrow size distribution with a normal morphology are present in the sample. The majority of the nanoparticles observed in the micrographs are nearly spherical and well dispersed, with a mean particle size of 3 ± 0.4 nm (N = 150) (Fig. 4(b)), where 3 is the mean size, 0.4 is the standard
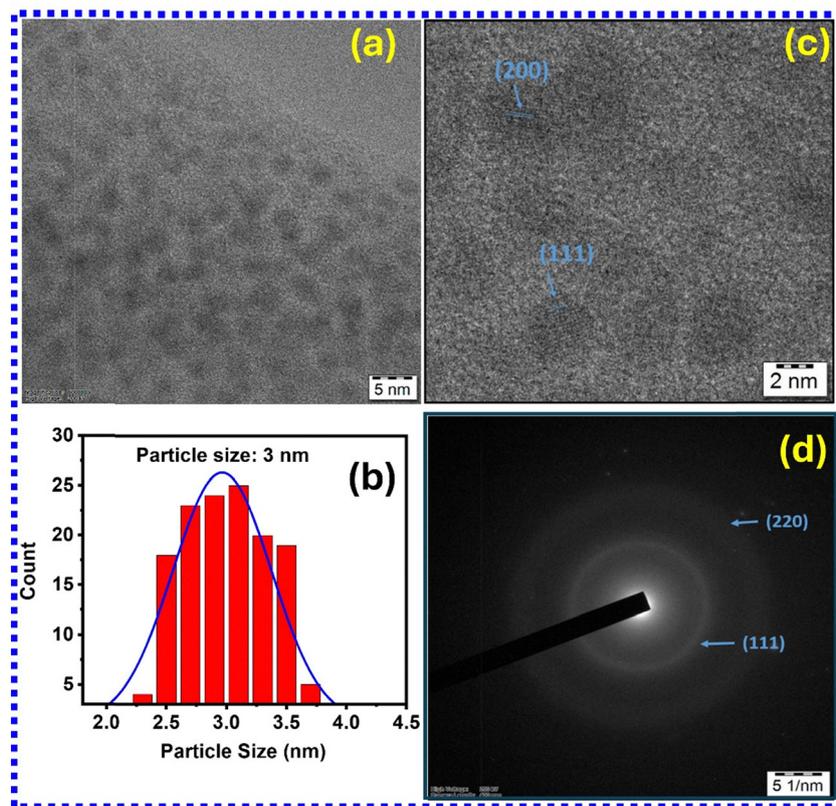

Fig. 4 Morphological and microstructural characterization of the synthesized Cu NPs. (a) TEM image of the isolated nanoparticles. (b) Particle size distribution histogram. (c) High-resolution TEM (HRTEM) image of the Cu NPs. (d) Selected area electron diffraction (SAED) pattern.

deviation, and N is the number of particles measured. The particle size is observed by using ImageJ software, and the mean size of the particles is shown in the histogram. The lattice planes (111) and (200) are observed in the HR-TEM image (Fig. 4(c)), which also supports the Cu phase of the sample. The diffraction rings in the selected area electron diffraction (SAED) pattern show that the crystalline phase of the nanoparticles is present in the sample (Fig. 4(d)). The SAED pattern and lattice planes display distinct diffraction rings, consistent with those of metallic copper, further corroborating the XRD data.

The nitrogen adsorption–desorption isotherms and pore size distribution analyses provide insight into the textural properties of the synthesized Cu NPs. The isotherms shown in Fig. 5(a) and (b) exhibit a gradual increase in adsorption volume with rising relative pressure, followed by a more pronounced uptake near $P/P_0 \sim 0.9$–1.0. This behavior is characteristic of type IV isotherms, which are typically associated with mesoporous materials. The presence of a hysteresis loop between the adsorption and desorption branches further supports the mesoporous nature and suggests capillary condensation occurring within the pores at higher relative pressures. Fig. 5(c) displays the Barrett–Joyner–Halenda (BJH) pore size distribution derived from the desorption branch of the isotherm. The graph indicates that the pore volume is primarily

concentrated in pores with radii ranging from approximately 2 to 20 nm, consistent with the definition of mesopores. A secondary contribution is observed at larger pore radii, possibly arising from interparticle voids or aggregations of nanoparticles. Fig. 5(d) shows the cumulative pore volume plot, indicating that the majority of the accessible pore volume is contributed by smaller mesopores, with a steep initial rise followed by a plateau as the pore radius increases. This profile further highlights that the synthesized Cu NPs possess significant nanoscale porosity.

Overall, the nitrogen adsorption–desorption analysis confirms that the Cu NPs prepared *via* tartaric acid-mediated metal displacement exhibit mesoporous textural characteristics, providing a high surface area and pore volume that are beneficial for applications such as catalysis and adsorption-based processes. The surface area of Cu NPs was found to be 7.7 m^2 g^{-1}.[71]

Photocatalytic activity studies. The photocatalytic efficiency of the Cu NPs depends on their narrow bandgap, tunable electronic properties, and ability to generate ROS. This study highlights the role of Cu NPs in degrading organic pollutants under visible light. Surface morphology, including size, shape, porosity, and crystallinity, significantly affects light absorption and charge dynamics. Smaller Cu NPs, with higher surface area, offer more active sites for dye degradation, as confirmed by
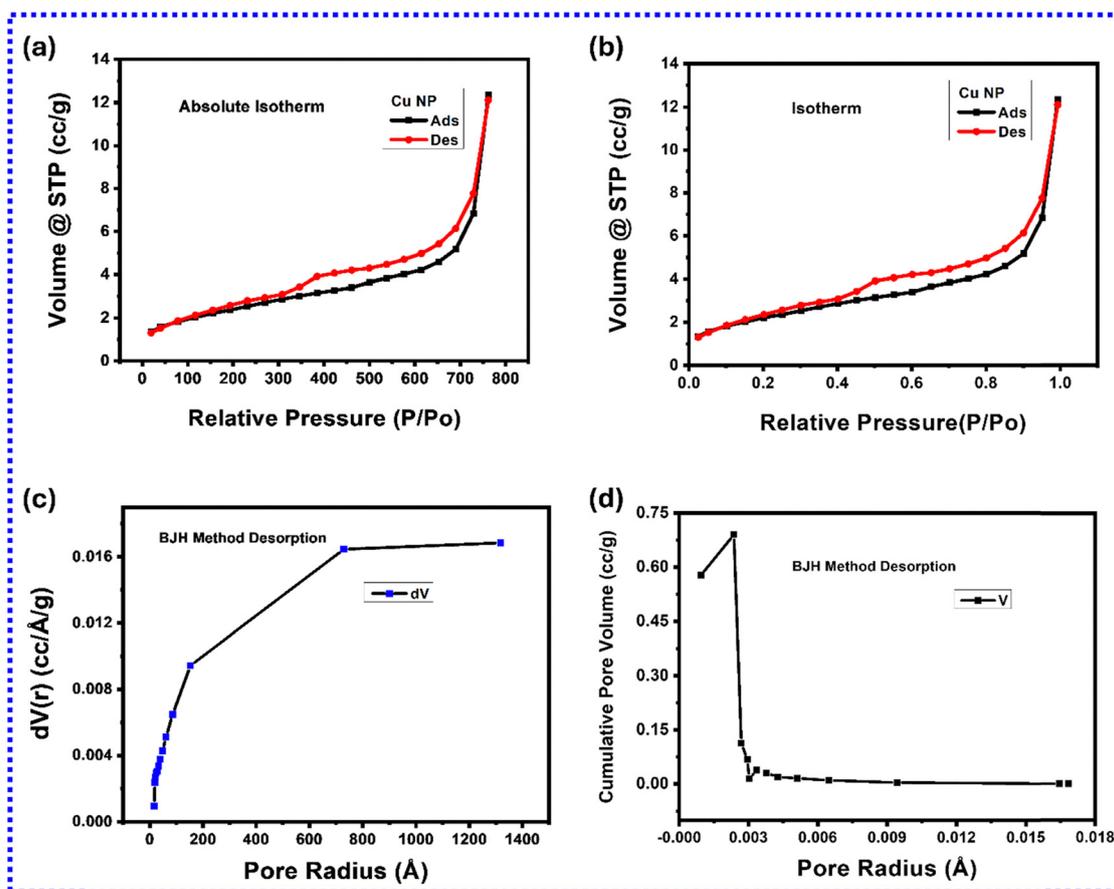

Fig. 5 BET analysis of the synthesized Cu NPs. (a) Absolute isotherm. (b) Isotherm in normalized form. (c) Barrett−Joyner−Halenda (BJH) pore size distribution. (d) The cumulative pore volume plot.

TEM analysis. Moreover, the Cu^0/Cu^+ redox cycle plays a key role in electron shuttling, boosting ROS generation and overall photocatalytic efficiency.[72]

Fig. 6(a) and (b) present the UV-Vis spectra of MB dye and RB dye after 180 minutes of catalytic treatment. A gradual reduction in the main absorption peaks was observed, indicating the breakdown of key chromophore groups responsible for dye coloration. Likewise, the prepared Cu NP photocatalytic studies were examined against the RB dye solution. The efficiency plot (C/C_0) of the MB dye and RB dye solution is represented in Fig. 6(c). The efficiency plot describes the Cu NPs, which showed the maximum degrading ability. The degradation efficiencies of Cu NPs were 88.1%, respectively. These findings highlight the superior photocatalytic performance of Cu NPs. Under the same conditions, the degrading efficiencies of the Cu NPs were 97.9% (Fig. 6(d)).
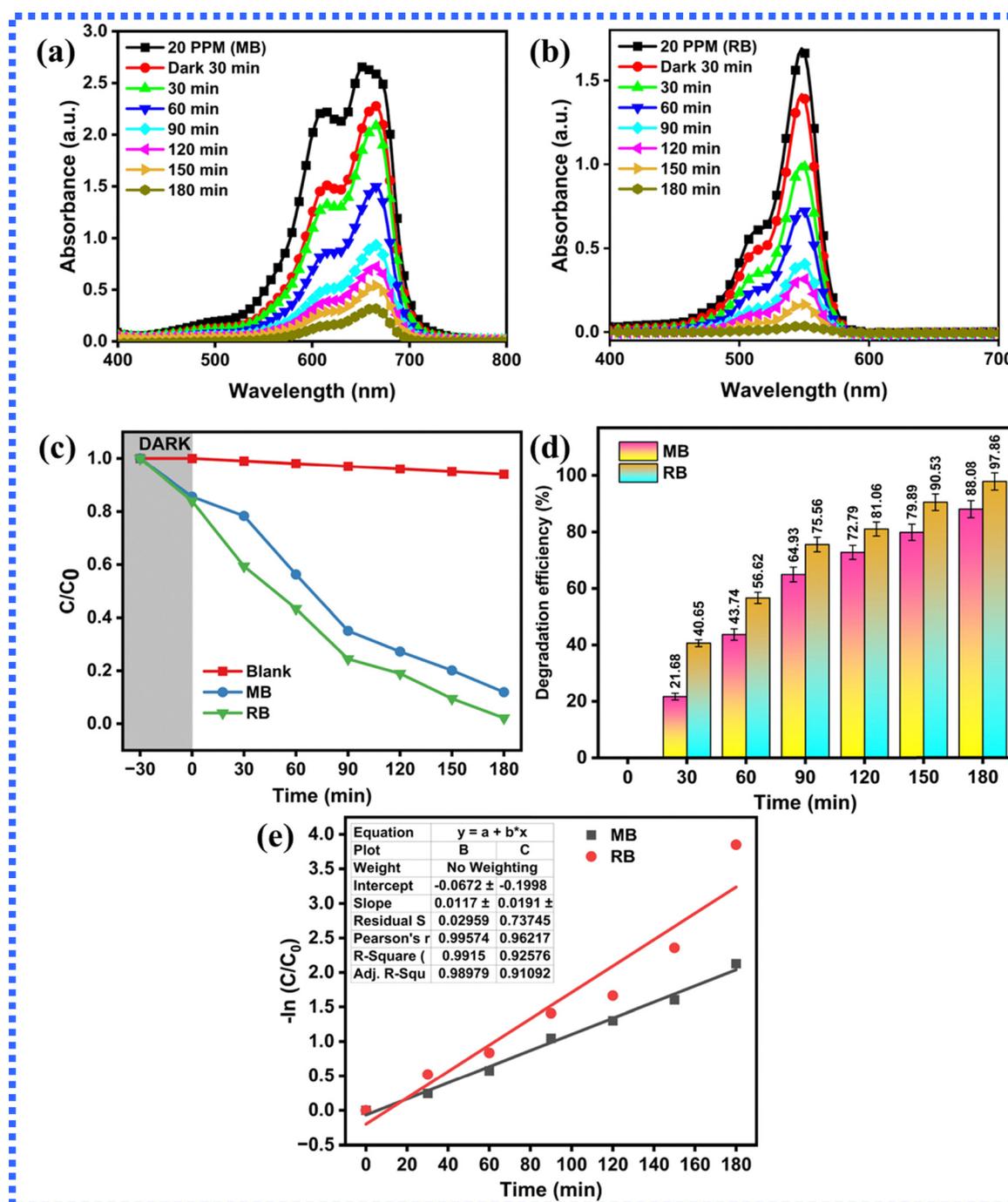

Fig. 6 Photocatalytic degradation by Cu nanoparticles: (a) MB, (b) RB, (c) efficiency plot (C/C_0), (d) degradation efficiency, and (e) degradation kinetic study of MB and RB dye.

Table 2 Dehydration parameters of Cu NPs against RB and MB dye solution

S. no.	Name of dye solution	Concentration of dye solution (ppm)	Light source	Degradation efficiency (%)	K (min^{-1})	R^2
1	RB	20	Visible	97.9	0.043	0.99
2	MB	20	Visible	88.1	0.026	0.92

Fig. 6(e) clearly illustrates the kinetic study of the degradation process, confirming that it follows first-order kinetics. While catalyst concentration plays a crucial role in enhancing photocatalytic activity, an excessive amount can hinder light absorption, thereby limiting efficiency. The corresponding pseudo-first-order rate constants (k) were 0.043 min^{-1} (R^2 = 0.99) for RB and 0.026 min^{-1} (R^2 = 0.92) for MB and shown in Table 2.[73–75]

3.3. Photodegradation of a dye mixture

Fig. 7(a) and (b) represents the study of the photodegradation of a mixture of MB and RB using Cu NPs, demonstrating the efficient catalytic activity of Cu-based nanomaterials in the degradation of organic dyes under visible light irradiation. The experiments were conducted on the solution mixture with samples taken at every 30 min interval. After 180 minutes of light irradiation, the UV-Vis spectrophotometric analysis confirmed a progressive reduction in absorbance at λ-max 663 nm (MB) and 545 nm (RB), indicating effective dye degradation. Cu NPs significantly improved the degradation of MB and RB due to their LSPR effect, which enhances light absorption and electron transfer.[76,77] In the mixed dye degradation study, potential spectral interference between MB and RB was carefully considered. As shown in Fig. 7(a), both dyes exhibit strong absorbance in the visible region, MB at approximately 663 nm and RB at 545 nm, leading to partial spectral overlap in the UV-Vis absorption spectra. To accurately monitor the degradation of each dye, their characteristic absorption maxima (663 nm for monomeric MB and 545 nm for RB) were independently tracked throughout the photocatalytic process.[78] These

wavelengths were selected for their minimal overlap and high sensitivity to concentration changes. In cases of slight overlap, spectral deconvolution was carried out using baseline correction and absorbance subtraction techniques to isolate and quantify the individual contributions of each dye. This approach enabled a precise evaluation of the degradation efficiency, as illustrated in Fig. 7(b), for the mixed dye system. Cu NPs offer a promising, cost-effective, and environmentally friendly approach for the photodegradation of MB and RB, paving the way for their application in large-scale wastewater treatment and environmental remediation.

3.4. Role of active species

When exposed to visible light, photons are absorbed by the photoactive catalyst, which creates electron–hole pairs as charge carriers. These charge carriers facilitate the production of reactive oxygen species (ROS), which play a critical role in photodegradation.[79,80] Typically, three types of ROS are generated, and it is essential to identify and control the dominant ROS responsible for the degradation mechanism.[81] Scavenger experiments were conducted to elucidate the photodegradation pathway of dyes over the Cu NP catalyst, providing valuable insights into the specific ROS involved and their contributions to the degradation process. The scavenger reagents ethylenediaminetetraacetic acid (EDTA), methanol, and p-benzoquinone (BQ) are h$^+$ scavengers, $^{\bullet}$OH scavengers, and O$_2^{\bullet-}$ scavengers, respectively. They were included in the reagent to inhibit the action of h$^+$, $^{\bullet}$OH, and O$_2^{\bullet-}$. Fig. 8(a)–(c) illustrates the percentage degradation in the presence of various scavengers. The scavenger studies revealed that adding BQ and EDTA significantly suppressed the degradation efficiency of both dyes, indicating their role in quenching specific reactive species of superoxide radical and hole involved in the photodegradation process.[82] The structure and morphology of the catalyst are critical factors influencing its performance under visible light illumination. In this study, the Cu NPs resulted in enhanced visible light absorption and an increased number of surface-active sites, which collectively contributed to the improved degradation efficiency of MB and RB
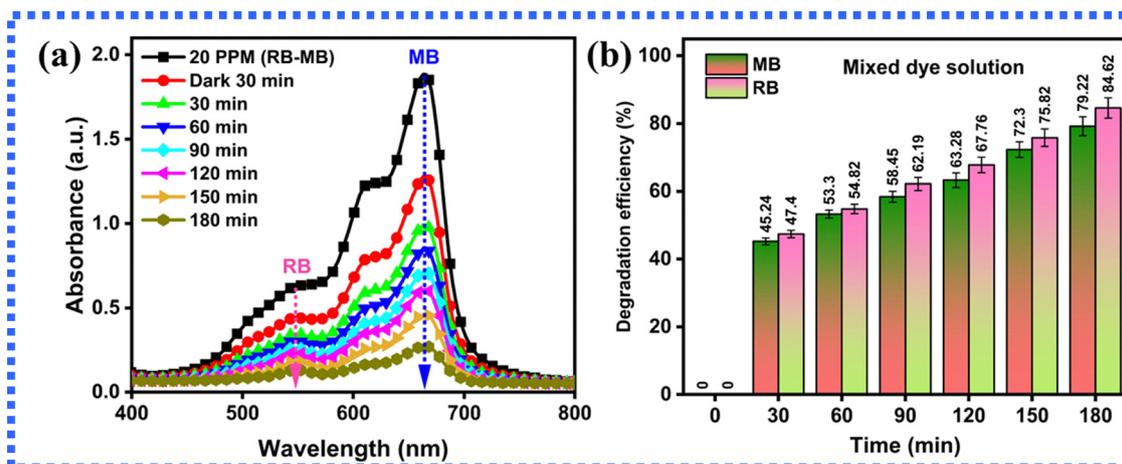

Fig. 7 (a) UV-visible spectra of photocatalytic degradation of mixed dyes of (RB-MB) by Cu NPs and (b) degradation efficiency for mixed dyes (RB-MB).
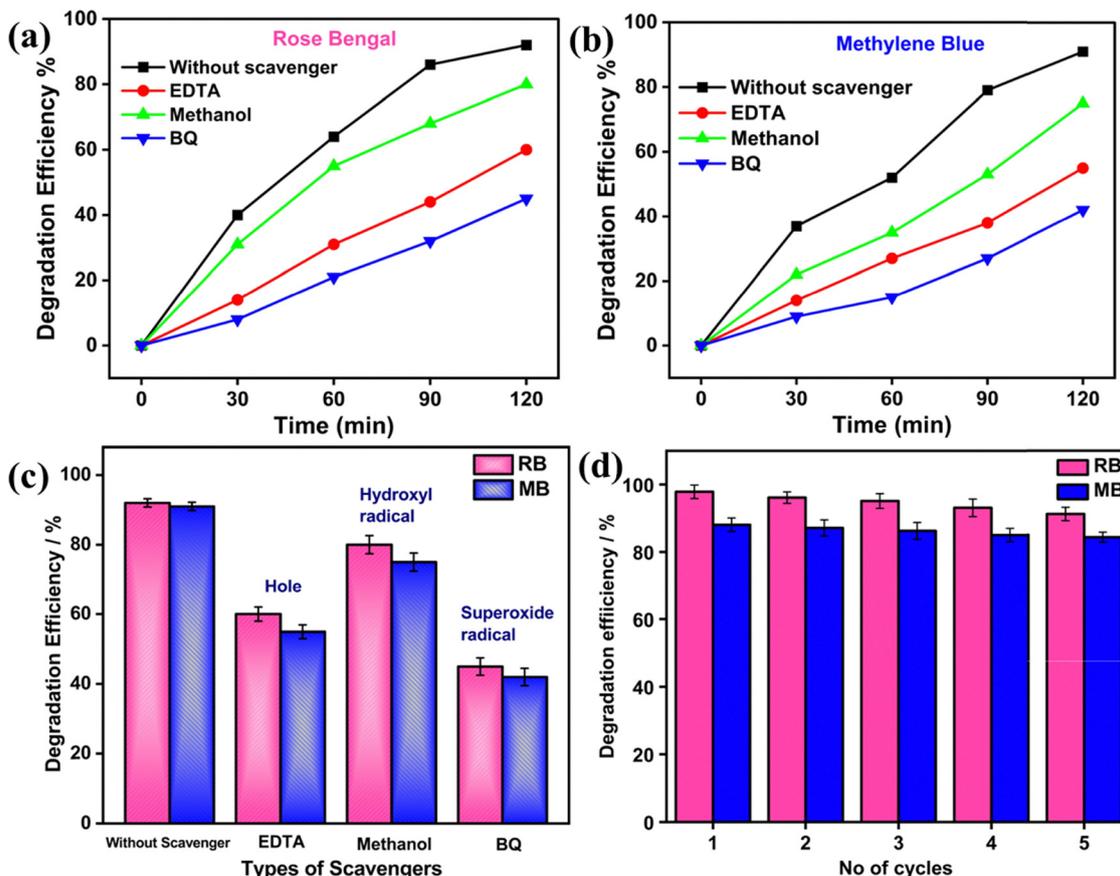
Fig. 8 (a)–(c) Scavenger study, and (d) reusability results of Cu NPs for RB and MB dye.

dyes. Furthermore, the reusability of the Cu NP catalyst was reviewed over five consecutive cycles, as shown in Fig. 8(d), demonstrating its stability and potential for practical applications in wastewater treatment. But, this minor drop is attributed to catalyst loss during recovery and accumulation of intermediate products on the surface.

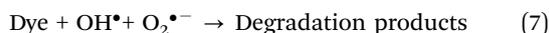The photocatalytic mechanisms are as mentioned below,[80,83]

(i) Production of excitons

$$\text{Cu NPs} + h\nu \rightarrow \text{h}^+ \text{ (VB)} + \text{e}^- \text{ (CB)} \qquad (3)$$
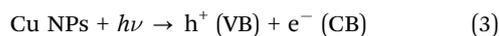
(ii) Hydroxyl radical generation

$$\text{OH}^- + \text{h}^+ \rightarrow \text{OH}^\bullet \qquad (4)$$

$$\text{H}_2\text{O} + \text{h}^+ \rightarrow \text{OH}^\bullet + \text{H}^+ \qquad (5)$$
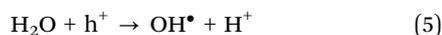
(iii) Superoxide radical generation

$$\text{O}_2 + \text{e}^- \rightarrow \text{O}_2^{\bullet-} \qquad (6)$$

(iv) Degradation of dye molecules

$$\text{Dye} + \text{OH}^\bullet + \text{O}_2^{\bullet-} \rightarrow \text{Degradation products} \qquad (7)$$

The Cu NPs act as efficient photocatalysts in the degradation of organic dyes like MB and RB due to their ability to generate ROS. Primarily, the Cu NPs, when exposed to light, promote

electron transfer to oxygen, generating superoxide radicals and $\text{O}_2^{\bullet-}$ initiates dye degradation by attacking conjugated structures in MB and RB. Superoxide anion radicals are highly reactive and break down dye molecules into smaller, less harmful fragments. They attack aromatic rings and chromophores, leading to the loss of color in the MB and RB solutions. Cu NPs adsorb dye molecules, facilitating direct electron transfer (DET), which leads to the breakdown of dye molecules via reductive cleavage. Rough or mesoporous Cu NPs provide more defect sites, which can act as traps for charge carriers, reducing electron–hole recombination. The crystallographic facets of Cu NPs impact their reactivity and electron transfer properties, which improve visible-light absorption and photocatalytic efficiency. Fig. 9 shows the schematic diagram and the possible degradation mechanism of the photocatalytic dye degradation. Furthermore, Table 2 presents a comparative summary of recently reported Cu-based photocatalysts, highlighting their degradation efficiencies for dye degradation.

The degradation products of the MB and RB dyes were investigated using LC-MS analysis.[84,85] As shown in Fig. 10, UV-Vis chromatographic results of MB dye revealed a prominent peak at 11.873 min before treatment, confirming the presence of intact MB. After photocatalysis, this peak significantly diminished, with new peaks emerging at 4.323, 12.068, 13.714, and 28.747 min, indicating the formation of intermediate and final
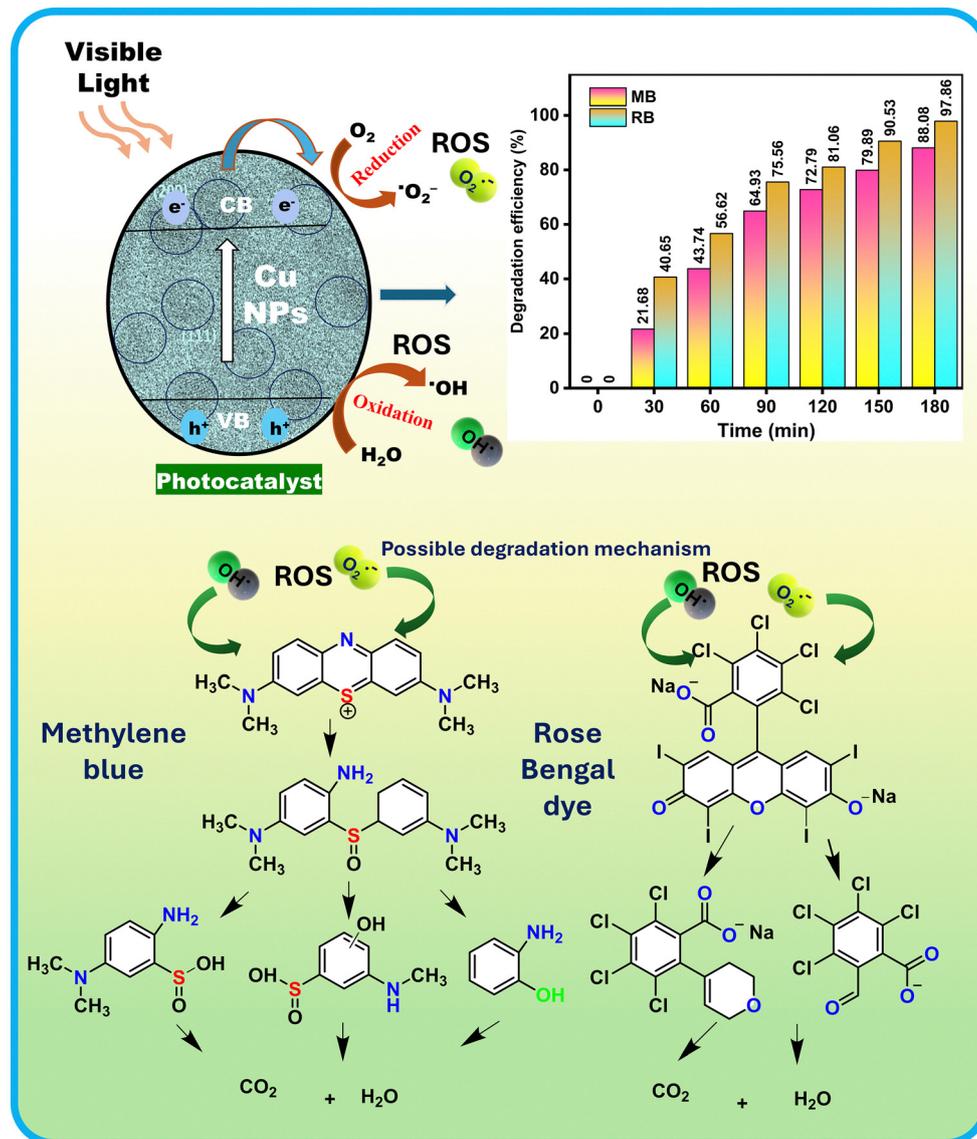
Fig. 9 Schematic diagram and possible degradation mechanism of the photocatalytic dye degradation.

degradation products. Furthermore, total ion chromatograms (TIC) from LC further support this observation. Prior to treatment, major peaks at 11.933, 11.123, and 10.109 min, along with 27.295 and 29.099 min, correspond to undegraded MB species. Post-treatment spectra showed the disappearance of these peaks and the appearance of new signals at 11.490, 12.091, and 15.751 min, confirming effective degradation and partial mineralization. Mass spectra analysis (Fig. S2) also support this conclusion. A dominant peak at m/z = 743.5 (RT = 11.123 min) in the untreated sample corresponds to intact MB or its dimer/adduct form. After photocatalysis, this peak disappears, and new low-mass fragments at m/z = 122.10, 143.10, 204.10, and 259.10 appear, representing oxidative degradation products. These changes confirm the breakdown of MB into smaller species and the high efficiency of the photocatalyst in dye degradation.

Similarly, the photocatalytic degradation of RB dye was systematically investigated using LC-MS analysis. As shown in Fig. S3, the total ion chromatogram (TIC) before treatment exhibited sharp and prominent peaks at 10.09, 11.11, 26.183, and 29.19 min, which are attributed to the intact RB and its associated species. After photocatalytic treatment, these peaks were significantly reduced. New peaks emerged at 2.175, 3.625, 25.704, and 29.108 min, indicating the formation of intermediate degradation products and partial mineralization of RB. Mass spectral analysis further validates this transformation (Fig. S4). Prior to degradation, a strong peak at m/z = 701.5 (RT = 11.109 min) was observed, corresponding to intact RB molecules. Additionally, signals at m/z = 340.4 and 679.5 support the presence of unaltered dye species. Post-photocatalysis, these characteristic peaks vanished, and new fragment ions appeared at m/z = 163.2, 201.1, 259.1, 284.4, 369.3, and 473.3. These low-mass ions are indicative of oxidative cleavage and breakdown of RB molecules into smaller organic fragments. Overall, the disappearance of the parent dye peak and the formation of distinct lower-mass fragments confirm
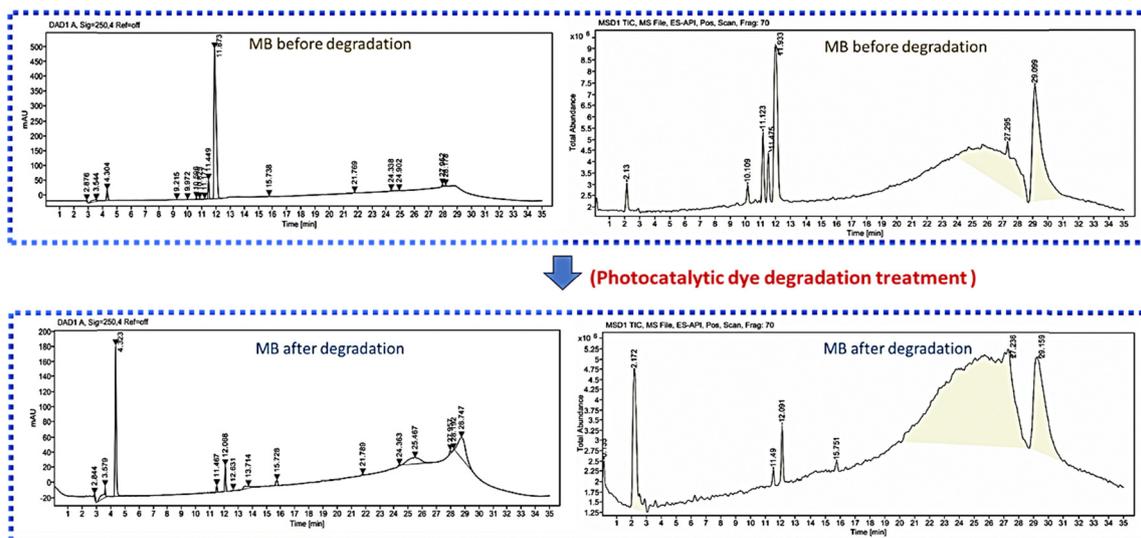
Fig. 10 LC-MS analysis of methylene blue (MB) dye before and after photocatalytic degradation.

Table 3 Comparison of the photocatalytic activity of the Cu NPs for various dyes

Catalyst	Dye	Volume of dye. (mL)	Catalyst conc. (mg)	Light source	Time duration (min)	Efficiency (%)	Ref.
CuO	Methylene blue	10	10	Sun light	135	92	86
Cu NPs	Direct blue	100	100	Sun light	300	91.53	87
Cu–TiO$_2$	Methylene blue	60	10	Visible	120	99	88
Ag$_{25}$–Cu$_{75}$	Methylene blue	48	10	Visible	70	70	89
Cu NPs	Methylene blue	40	10	Sun light	120	81	87
KA@CP-S	Rose bengal	25	40	Room light	150	76.1	90
5%Zr–CuFe$_2$O	Rose bengal	100	100	Visible	120	88	91
CuO	Rose bengal	10	10	UV	120	92	92
Cu NPs	Methylene blue, (RB-MB)	50	25	Visible	180	88.08, 97.86 & 79.22–84.62	This work

the successful photocatalytic degradation of RB dye and highlight the efficiency of the employed photocatalyst in breaking down complex dye pollutants. The detailed comparison of the photocatalytic activity of the Cu NPs for various dyes is presented in Table 3.

4. Conclusions

In summary, this study demonstrates a clean, low-cost, environmentally friendly, and efficient strategy for synthesizing pure metallic Cu NPs using tartaric acid-assisted metal displacement with aluminum under mild aqueous conditions. The resulting nanoparticles exhibit uniform nanoscale dimensions, sharp crystallinity, and exceptional stability against oxidation, as confirmed by comprehensive structural and surface analyses. Their strong localized surface plasmon resonance and high surface area enable excellent photocatalytic performance, achieving rapid and efficient degradation of organic dyes under visible light irradiation. In particular, the synthesized Cu nanoparticle photocatalyst exhibited high photocatalytic efficiency under visible light, achieving 97.9% degradation of rose bengal (k = 0.043 min^{-1}) and 88.1% for methylene blue (k = 0.026 min^{-1}), confirming its strong activity and favorable

kinetics. LC-MS analysis confirmed the successful photocatalytic degradation of both methylene blue (MB) and rose bengal (RB) dyes. Disappearance of the parent dye peaks and emergence of low-mass fragments indicate complete breakdown and formation of intermediate degradation products. The unique combination of structural purity, oxidation resistance, and catalytic activity underscores the potential of these Cu NPs as sustainable materials for advanced wastewater treatment and environmental remediation applications.

Author contributions

RK: investigation, methodology, data curation, formal analysis, writing – original draft. GM: investigation, methodology, formal analysis, data curation, writing – original draft. NV: investigation, methodology, formal analysis, writing – original draft. SVS: investigation, methodology, formal analysis, writing – original draft. DP: investigation, methodology, formal analysis, writing – original draft. ST: investigation, methodology, formal analysis, writing – original draft. RKR: formal analysis, funding acquisition, methodology, resources, supervision, validation, visualization, writing – review & editing. HD: formal analysis, funding acquisition, methodology, resources, supervision,

validation, visualization, writing – review & editing. MD: conceptualization, data curation, formal analysis, project administration, resources, software, validation, visualization, writing – original draft, writing – review & editing. AP: conceptualization, data curation, formal analysis, project administration, resources, software, validation, visualization, writing – original draft, writing – review & editing. CRM: conceptualization, data curation, formal analysis, project administration, resources, software, validation, visualization, writing – original draft, writing – review & editing. UKK: conceptualization, data curation, formal analysis, funding acquisition, methodology, project administration, resources, supervision, validation, visualization, writing – original draft, writing – review & editing.

Conflicts of interest

There are no conflicts to declare.

Data availability

The data supporting this article have been included as part of the supplementary information (SI). Supplementary information is available. Fig. S1 describes XRD patterns of Cu NPs immediately after synthesis and after 45 days. Fig. S2–S4 describes, LC-MS analysis of Rose Bengal (RB), methylene blue (MB) before and after photocatalytic degradation. See DOI: https://doi.org/10.1039/d5ma00769k.

References

1 E. K. Nti, S. J. Cobbina, E. E. Attafuah, L. D. Senanu, G. Amenyeku, M. A. Gyan, D. Forson and A. R. Safo, *Heliyon*, 2023, **9**, e18170.

2 C. Parra-López, S. Ben Abdallah, G. Garcia-Garcia, A. Hassoun, H. Trollman, S. Jagtap, S. Gupta, A. Aït-Kaddour, S. Makmuang and C. Carmona-Torres, *Agric. Water Manage.*, 2025, **309**, 109347.

3 M. F. Hussein, M. F. Mubarak, A. M. Al-Sirhani and R. Hosny, *Discover Appl. Sci.*, 2024, **6**, 519.

4 Y.-L. Luo, Y.-R. Pan, X. Wang, Z.-Y. Wang, G. Daigger, J.-X. Ma, L.-H. Tang, J. Liu, N.-Q. Ren and D. Butler, *Nat. Commun.*, 2025, **16**, 1269.

5 V. Rocha, A. Lago, B. Silva, Ó. Barros, I. C. Neves and T. Tavares, *Environ. Sci.: Nano*, 2024, **11**, 36–60.

6 A. Kaki, G. Maharana, N. Madathil, V. Mahesh, K. U. Kumar, P. J. Daniel and R. K. Rajaboina, *Adv. Sustainable Syst.*, 2025, e00235.

7 R. Kumar, M. Qureshi, D. K. Vishwakarma, N. Al-Ansari, A. Kuriqi, A. Elbeltagi and A. Saraswat, *Case Stud. Chem. Environ. Eng.*, 2022, **6**, 100219.

8 F. Wang, L. Xiang, K. Sze-Yin Leung, M. Elsner, Y. Zhang, Y. Guo, B. Pan, H. Sun, T. An, G. Ying, B. W. Brooks, D. Hou, D. E. Helbling, J. Sun, H. Qiu, T. M. Vogel, W. Zhang, Y. Gao, M. J. Simpson, Y. Luo, S. X. Chang, G. Su, B. M. Wong, T.-M. Fu, D. Zhu, K. J. Jobst, C. Ge, F. Coulon, J. D. Harindintwali, X. Zeng, H. Wang, Y. Fu, Z. Wei, R. Lohmann, C. Chen, Y. Song, C. Sanchez-Cid, Y. Wang, A. El-Naggar, Y. Yao, Y. Huang, J. Cheuk-Fung Law, C. Gu, H. Shen, Y. Gao, C. Qin, H. Li, T. Zhang, N. Corcoll, M. Liu, D. S. Alessi, H. Li, K. K. Brandt, Y. Pico, C. Gu, J. Guo, J. Su, P. Corvini, M. Ye, T. Rocha-Santos, H. He, Y. Yang, M. Tong, W. Zhang, F. Suanon, F. Brahushi, Z. Wang, S. A. Hashsham, M. Virta, Q. Yuan, G. Jiang, L. A. Tremblay, Q. Bu, J. Wu, W. Peijnenburg, E. Topp, X. Cao, X. Jiang, M. Zheng, T. Zhang, Y. Luo, L. Zhu, X. Li, D. Barceló, J. Chen, B. Xing, W. Amelung, Z. Cai, R. Naidu, Q. Shen, J. Pawliszyn, Y. Zhu, A. Schaeffer, M. C. Rillig, F. Wu, G. Yu and J. M. Tiedje, *Innovation*, 2024, **5**, 100612.

9 M. F. Mubarak, H. Selim, H. B. Hawash and M. Hemdan, *Environ. Sci. Pollut. Res. Int.*, 2024, **31**, 2297–2313.

10 S. F. Ahmed, M. Mofijur, S. Nuzhat, A. T. Chowdhury, N. Rafa, M. A. Uddin, A. Inayat, T. M. I. Mahlia, H. C. Ong, W. Y. Chia and P. L. Show, *J. Hazard. Mater.*, 2021, **416**, 125912.

11 J. Shamshad and R. Ur Rehman, *Environ. Sci.: Adv.*, 2025, **4**, 189–222.

12 S. Gupta, Y. Mittal, R. Panja, K. B. Prajapati and A. K. Yadav, *Current Developments in Biotechnology and Bioengineering: Strategic Perspectives in Solid Waste and Wastewater Management*, 2021, pp. 47–75.

13 P. Mondal, A. Nandan, S. Ajithkumar, N. A. Siddiqui, S. Raja, A. K. Kola and D. Balakrishnan, *Environ. Res.*, 2023, **232**, 116071.

14 G. Ramalingam, N. Perumal, A. K. Priya and S. Rajendran, *Chemosphere*, 2022, **300**, 134391.

15 R. Ahesteh, A. Nezamzadeh-Ejhieh and S. N. Mirsattari, *Mater. Adv.*, 2025, **6**, 4046–4061.

16 R. Fazaeli, H. Aliyan, A. Nezamzadeh-Ejhieh and D. Richeson, *Surf. Interfaces*, 2024, **52**, 104877.

17 M. Rezaei, A. Nezamzadeh-Ejhieh and A. R. Massah, *ACS Omega*, 2024, **9**, 6093–6127.

18 M. Rezaei, A. Nezamzadeh-Ejhieh and A. R. Massah, *Energy Fuels*, 2024, **38**, 7637–7664.

19 M. F. Al-Hakkani, *SN Appl. Sci.*, 2020, **2**, 1–20.

20 A. R. Indhu, C. Dharanya and G. Dharmalingam, *Plasmonics*, 2023, **19**, 1303–1357.

21 A. K. El-Sawaf, A. A. Nassar, A. A. El Aziz Elfiky and M. F. Mubarak, *Polym. Bull.*, 2024, **81**, 12451–12476.

22 H. Derikvandi, M. Vosough and A. Nezamzadeh-Ejhieh, *Environ. Sci. Pollut. Res.*, 2020, **27**, 27582–27597.

23 H. Derikvandi, M. Vosough and A. Nezamzadeh-Ejhieh, *Int. J. Hydrogen Energy*, 2021, **46**, 2049–2064.

24 S. Raina, A. Roy and N. Bharadvaja, *Environ. Nanotechnol., Monit. Manage.*, 2020, **13**, 100278.

25 A. Nezamzadeh-Ejhieh and H. Zabihi-Mobarakeh, *J. Ind. Eng. Chem.*, 2014, **20**, 1421–1431.

26 M. Karimi-Shamsabadi and A. Nezamzadeh-Ejhieh, *J. Mol. Catal. A: Chem.*, 2016, **418–419**, 103–114.

27 R. Ahesteh, A. Nezamzadeh-Ejhieh and S. N. Mirsattari, *Mater. Adv.*, 2025, **6**, 4046–4061.

28 S. C. Priya, S. Vijayalakshmi, S. G. Raghavendra, S. Yildizhan and J. Ranjitha, *Mater. Today Proc.*, 2023, **80**, 3075–3081.

29 T. Kaushik, S. Ghosh, T. Dolkar, R. Biswas and A. Dutta, *ACS Nanosci. Au*, 2024, **4**, 273–289.

30 M. B. Gawande, A. Goswami, F.-X. Felpin, T. Asefa, X. Huang, R. Silva, X. Zou, R. Zboril and R. S. Varma, *Chem. Rev.*, 2016, **116**, 3722–3811.

31 C. Y. Toe, Z. Zheng, H. Wu, J. Scott, R. Amal and Y. H. Ng, *Angew. Chem., Int. Ed.*, 2018, **57**, 13613–13617.

32 Y. Kobayashi, S. Ishida, K. Ihara, Y. Yasuda, T. Morita and S. Yamada, *Colloid Polym. Sci.*, 2009, **287**, 877–880.

33 A. H. Ragab, B. S. Mettwally, M. F. Mubarak, A. Al-Ghamdi and M. Hemdan, *J. Inorg. Organomet. Polym. Mater.*, 2024, **34**, 1491–1505.

34 A. Norouzi, A. Nezamzadeh-Ejhieh and R. Fazaeli, *Mater. Sci. Semicond. Process.*, 2021, **122**, 105495.

35 A. Bunge, T. Radu, G. Borodi, S. Boca and A. Nan, *Polymers*, 2023, **15**, 4472.

36 T. Muthukumaran and J. Philip, *Adv. Colloid Interface Sci.*, 2024, **334**, 103314.

37 A. K. Sidhu, N. Verma and P. Kaushal, *Front. Nanotechnol.*, 2022, **3**, 801620.

38 P. Savchenko, D. Zelikovich, H. Elgavi Sinai, R. Baer and D. Mandler, *J. Am. Chem. Soc.*, 2024, **146**, 22208–22219.

39 N. Jayarambabu, A. Akshaykranth, T. Venkatappa Rao, K. Venkateswara Rao and R. Rakesh Kumar, *Mater. Lett.*, 2020, **259**, 126813.

40 N. K. Sharma, J. Vishwakarma, S. Rai, T. S. Alomar, N. AlMasoud and A. Bhattarai, *ACS Omega*, 2022, **7**, 27004–27020.

41 J. Ferro-Falla, L. S. Rowles, F. D. Arriaga and J. Plazas-Tuttle, *Water Cycle*, 2025, **6**, 473–484.

42 H. Cheng, C. Wang, D. Qin and Y. Xia, *Acc. Chem. Res.*, 2023, **56**, 900–909.

43 X. Kong, H. Wu, K. Lu, X. Zhang, Y. Zhu and H. Lei, *ACS Appl. Mater. Interfaces*, 2023, **15**, 41205–41223.

44 N. Sarwar, U. Bin Humayoun, M. Kumar, S. F. A. Zaidi, J. H. Yoo, N. Ali, D. I. Jeong, J. H. Lee and D. H. Yoon, *J. Cleaner Prod.*, 2021, **292**, 125974.

45 A. H. Ragab, N. F. Gumaah, A. A. El Aziz Elfiky and M. F. Mubarak, *BMC Chem.*, 2024, **18**, 121.

46 L. Karimi, S. Zohoori and M. E. Yazdanshenas, *J. Saudi Chem. Soc.*, 2014, **18**, 581–588.

47 S. Verma, K. Vikrant and K.-H. Kim, *Environ. Sci.: Nano*, 2023, **10**, 2035–2052.

48 Z. Kalaycıoğlu, B. Özuğur Uysal, Ö. Pekcan and F. B. Erim, *ACS Omega*, 2023, **8**, 13004–13015.

49 H. D. Tran, D. Q. Nguyen, P. T. Do and U. N. P. Tran, *RSC Adv.*, 2023, **13**, 16915–16925.

50 M. Arifur, R. Khan and M. A. Rashed, *Sci. Rep.*, 2025, **15**, 1–10.

51 N. A. Dhas, C. P. Raj and A. Gedanken, *Chem. Mater.*, 1998, **10**, 1446–1452.

52 M. Nadeem Ahmad, M. N. Anjum, F. Nawaz, S. Iqbal, M. J. Saif, T. Hussain, A. Mujahid, M. U. Farooq, M. Nadeem, A. Rahman, A. Raza (Late) and K. Shehzad, *Polym. Compos.*, 2018, **39**, 4524–4531.

53 R. Lu, W. Hao, L. Kong, K. Zhao, H. Bai and Z. Liu, *RSC Adv.*, 2023, **13**, 14361–14369.

54 M. Salavati-Niasari, F. Davar and N. Mir, *Polyhedron*, 2008, **27**, 3514–3518.

55 D. Mott, J. Galkowski, L. Wang, J. Luo and C.-J. Zhong, *Langmuir*, 2007, **23**, 5740–5745.

56 Y. Chan, V. Selvanathan, L.-H. Tey, Md Akhtaruzzaman, F. Anur, S. Djearamane, A. Watanabe and M. Aminuzzaman, *Nanomaterials*, 2022, **12**, 3589.

57 Y. Bin Chan, M. Aminuzzaman, L.-H. Tey, Y. F. Win, A. Watanabe, S. Djearamame and Md Akhtaruzzaman, *Materials*, 2023, **16**, 5421.

58 Q. Ding, L. Hang and L. Ma, *RSC Adv.*, 2018, **8**, 1753–1757.

59 A. Mao, M. Ding, X. Jin, X. Gu, C. Cai, C. Xin and T. Zhang, *J. Mol. Struct.*, 2015, **1079**, 396–401.

60 E. C. Le Ru, E. Blackie, M. Meyer and P. G. Etchegoin, *J. Phys. Chem. C*, 2007, **111**, 13794–13803.

61 M. Ganiga and J. Cyriac, *ChemPhysChem*, 2016, **17**, 2315–2321.

62 S. Thota, S. C. Kashyap, S. K. Sharma and V. R. Reddy, *Mater. Sci. Eng., B*, 2016, **206**, 69–78.

63 M. C. Biesinger, *Surf. Interface Anal.*, 2017, **49**, 1325–1334.

64 J. A. Creighton and D. G. Eadon, *J. Chem. Soc., Faraday Trans.*, 1991, **87**, 3881–3891.

65 A. K. El-Sawaf, S. R. El-Dakkony, M. A. Zayed, A. M. Eldesoky, A. A. Nassar, A. El Shahawy and M. F. Mubarak, *Results Eng.*, 2024, **22**, 101971.

66 Z. Issaabadi, M. Nasrollahzadeh and S. M. Sajadi, *J. Cleaner Prod.*, 2017, **142**, 3584–3591.

67 N. V. Suramwar, S. R. Thakare and N. T. Khaty, *Arabian J. Chem.*, 2016, **9**, S1807–S1812.

68 M. F. Al-Hakkani, *SN Appl. Sci.*, 2020, **2**, 1–20.

69 S. S. Gabr, E. Fayad, D. N. Binjawhar, M. Keshawy, I. E. T. El Sayed, T. A. Moghny and M. F. Mubarak, *Inorg. Chem. Commun.*, 2025, **178**, 114471.

70 A. K. El-Sawaf, S. R. El-Dakkony, M. A. Zayed, A. M. Eldesoky, A. A. Nassar, A. El Shahawy and M. F. Mubarak, *Results Eng.*, 2024, **22**, 101971.

71 S. S. Gabr, M. F. Mubarak, M. Keshawy, I. E. T. El Sayed and T. Abdel Moghny, *Appl. Water Sci.*, 2023, **13**, 230.

72 M. Hemdan, A. H. Ragab, H. A. El-Siaad, J. K. Kamel, N. F. Gumaah and M. F. Mubarak, *Environ. Sci. Pollut. Res.*, 2024, **31**, 66164–66183.

73 M. F. Mubarak, G. E. Khedr and H. M. El Sharkawy, *J. Alloys Compd.*, 2024, **999**, 175061.

74 S. Vahabirad and A. Nezamzadeh-Ejhieh, *J. Solid State Chem.*, 2022, **310**, 123018.

75 S. Sharafzadeh, J. Zolgharnein, A. Nezamzadeh-Ejhieh and S. D. Farahani, *Int. J. Hydrogen Energy*, 2025, **106**, 1429–1442.

76 L. Chen, H. Hu, Y. Chen, J. Gao and G. Li, *Mater. Adv.*, 2021, **2**, 907–926.

77 Y. Fang, B. Xu, S. Wang, H. Liu, J. Wang and M. Si, *Nanoscale*, 2024, **16**, 9748–9753.

78 S. Senobari and A. Nezamzadeh-Ejhieh, *Spectrochim. Acta, Part A*, 2018, **196**, 334–343.

79 B. E. Nagay, S. S. Malheiros, M. H. R. Borges, C. Aparicio, J. J. J. P. van den Beucken and V. A. R. Barão, *Bioact. Mater.*, 2025, **51**, 83–137.

80 S. Banerjee, S. C. Pillai, P. Falaras, K. E. O'Shea, J. A. Byrne and D. D. Dionysiou, *J. Phys. Chem. Lett.*, 2014, **5**, 2543–2554.

81 Z. Bi, W. Wang, L. Zhao, X. Wang, D. Xing, Y. Zhou, D. J. Lee, N. Ren and C. Chen, *Environ. Res.*, 2024, **260**, 119592.

82 G. Murugadoss, D. D. Kumar, M. R. Kumar, N. Venkatesh and P. Sakthivel, *Sci. Rep.*, 2021, **11**, 1–13.

83 M. Hemdan, A. H. Ragab, S. S. Elyan, M. A. Taher and M. F. Mubarak, *J. Cluster Sci.*, 2024, **36**, 2.

84 M. Aminuzzaman, P. S. Ng, W.-S. Goh, S. Ogawa and A. Watanabe, *Inorg. Nano-Met. Chem.*, 2019, **49**, 401–411.

85 M. Aminuzzaman, L. P. Ying, W.-S. Goh and A. Watanabe, *Bull. Mater. Sci.*, 2018, **41**, 50.

86 K. Dulta, G. Koşarsoy Ağçeli, P. Chauhan, R. Jasrotia, P. K. Chauhan and J. O. Ighalo, *Sustainable Environ. Res.*, 2022, **32**, 2.

87 M. Noman, M. Shahid, T. Ahmed, M. B. K. Niazi, S. Hussain, F. Song and I. Manzoor, *Environ. Pollut.*, 2020, **257**, 113514.

88 M. Ikram, E. Umar, A. Raza, A. Haider, S. Naz, A. Ul-Hamid, J. Haider, I. Shahzadi, J. Hassan and S. Ali, *RSC Adv.*, 2020, **10**, 24215–24233.

89 H. R. Tantawy, A. A. Nada, A. Baraka and M. A. Elsayed, *Appl. Surf. Sci. Adv.*, 2021, **3**, 100056.

90 Somnath, M. Ahmad and K. A. Siddiqui, *ACS Omega*, 2022, **7**, 41120–41136.

91 P. N. Dayana, M. J. Abel, P. F. H. Inbaraj, S. Sivaranjani, R. Thiruneelakandan and J. J. prince, *J. Cluster Sci.*, 2022, **33**, 1739–1749.

92 K. Parvathalu, K. Rajitha, B. Chandrashekar, K. Sathvik, K. Pranay Bhasker, B. Sreenivas, M. Pritam, P. Pushpalatha, K. Moses and P. Bala Bhaskar, *Plasmonics*, 2024, **19**, 825–834.